Response of Armour Steel Plates to localised Air Blast Load – A Dimensional Analysis

N Mehreganian[1], A S Fallah[2], G K Boiger[3], L A Louca[1]

1. Department of Civil & Environmental Engineering, Imperial College London, UK

2 Department of Aeronautics, Imperial College London, London, UK

3 ICP Institute of Computational Physics, Zurich University of Applied Sciences, Switzerland

ABSTRACT

We report on the results of dimensional analyses on the dynamic plastic response of square armour steel plates due to detonation of proximal cylindrical charges and ensued air blast loading. By assuming a generic function for the blast load, which is multiplicative comprising its spatial and temporal parts, a set of 14 dimensionless parameters, representative of the load and plate deformation, were identified and recast in the form of dimensionless functions of stand-off to charge diameter ratio. Parametric studies were performed using commercial code ABAQUS's module of Finite Element hydrocode using MMALE and MMAE techniques, and combined with regression analyses to quantify the dimensional parameters and the expressions for dimensionless functions. A few numerical studies with various FE mesh types were also performed to validate the transient deflections against the small-scale experiments. For pulse loading due to proximal charges of small orders of stand-off/charge diameter ratio, the magnitude of the transverse deflection increased abruptly with incremental decrease in stand-off, in contradistinction to the plate deformations at higher stand-offs where variations in displacement are smooth. This confirmed the existence of a stand-off at which a transition in behaviour takes place. For stand-off values less than charge diameter, a dimensionless energy absorbing effectiveness factor was considered to investigate the prediction of rupture in the plate corresponding to different charge masses. This factor is measured as a baseline parameter to predict, using solely numerical means, the blast loads which ensue rupture on full-scale prototypes.

1. INTRODUCTION

With an increased level of blast- and ballistic-related threats in the UK and around the globe in the recent years, design of the protective systems against such threats is of prime significance for civil, aeronautical, mechanical, defence and offshore engineers. Thus, efforts have been made to improve the blast- and ballistic-resistant performance of, for instance, transportation vehicles and civil structures. One vein through which this goal is achievable is the right choice of material. In fact, a considerable body of literature exists on

*Corresponding Author: arash.soleiman-fallah@imperial.ac.uk

the performance of steel, aluminium and composite plates subjected to uniformly impulsively (generated by far field explosives) blast, or localised blasts [1], [2] (generated by near field explosives), assessed numerically, experimentally [3]–[5] and theoretically. While the ballistic energy absorption capacity of some materials may be insufficient due to low ductility, low strength and weak hardening [6]–[8], other materials such as high strength ARMOX steel are more promising as they possess excellent ballistic performance due to high strength and ductility thus high energy absorbing capacity.

The experimental works of Ref.s [9], and [10] on uniformly impulsive loaded beams and plates, classified three failure modes as large inelastic deformation (Mode I), partial tearing (Mode II) or complete tearing and shear failure (Mode III). Similar modes of failure were also suggested for locally blast loaded plates [11], for which modes II and III correspond to partial tearing and capping at the centre, respectively.

Nurick and co-authors [4], [11]–[15] conducted considerable experimental studies on the response of mild steel plates to air blast loading, considering various parameters i.e. explosive mass and shape, plate geometry, and boundary conditions. A unifying approach was proposed through introduction of a single non-dimensional impulse parameter which allowed all data to collapse on a single curve to predict the permanent mid-point deformation.

Recently, the capability to study the physics of Fluid-Structure Interaction (FSI) is employed in several FE codes in order to provide a more realistic assessment of response to blast loading. Numerous studies of dynamic response using this technique are reported [16]–[22] which render a more realistic estimate of maximum and permanent transverse deflections achievable, closer to experimental results than the pure Lagrangian models. This can be useful since monitoring the transient deflection of the plate experimentally is notoriously difficult for which only a few experiments are available. For example, Aune et al [23] observed the transient deflection of thin ductile steel and aluminium plates subject to spherical air blast laods at various stand-offs using Digital Image Correlation. The DIC technique was also used by Spranghers et al [24] to validate their numerical models. Minimising the discrepancy between the observed experimental and predicted numerical models (inverse modelling approach), the authors iteratively updated the material parameters required for different phenomenological models characterising J2 plasticity of the aluminium plate.

1.1. Dimensional analyses

Dimensional analysis is a useful tool of generalisation and is used here to understand the phenomenon of blast loading and the physics of response of full-scale prototype through the study of geometrically similar small-scale models, without the necessity of conducting experiments on the former. The principle of scaling allows one to obtain a set of dimensionless parameters through multiplicative combination of defining variables used in numerical calculations or experimental measurements.

In the past, various researchers have used dimensionless parameters to investigate the elastic and/or plastic response of the structures to blast loads. Neuberger et al [25], [26] showed the normalised deflections predicted numerically on the small-scale model differed by marginally 7% from the results of four times as large full-scale prototype, the discrepency being due primarily to the change in material properties during scaling. Their experimental results, however, showed a 10% difference in peak deflections.

In other works of literature, the results of small-scale models have been cast in dimensionless form of impulse against characteristic response deflection (E.g. permanent or

maximum midpoint deflections); however, relying on impulse and deflections alone can be misleading, because in most practical cases, loading regime is dynamic rather than impulsive. Furthermore, the dimensional analyses in literature are devoid of proposing expressions to actually describe the air blast load, and are rather focused on providing expressions for the response of the structure.

The present article derives a set of dimensionless parameters that can fully describe both the loading variation (both spatial and temporal) and structural deformations. The derivation of dimensionless parameters is carried out in Section 2. The dimensional parameters are recast as dimensionless functions of loading- and structure-related design input parameters, namely, explosive mass and diameter, plate geometry, and material properties. The input parameters are implemented in the Finite Element package in Section 3. In Section 4 the results of numerical, experimental and theoretical analyses are presented, together with a discussion on the dimensionless impulse and energy absorbing effectiveness factor. The latter dimensionless parameters aid the designers to predict the blast load conditions that will ensue rupture in the structural elements. Finally, the concluding remarks are included in Section 5.

2. NON-DIMENSIONAL PARAMETERS

2.1. Localised blast load

A blast wave is generated by rapid release of energy due to detonation of a high explosive over a short period of time. In this work, the blast wave is assumed to be generated by a cylindrical explosive of certain mass M_e, having the diameter D_e, the heat energy per mass of Q_e which is placed at distance d from the target. This gives parameters defining the blast source uniquely as: M_e, d, D_e, and Q_e.

The blast wave pressure is assumed to be representable as a multiplicative decomposition of functions of the spatial part (also called load shape) and temporal part (pulse shape) [27], given in Eq. (1).

$$p(r,t) = p_0 p(r) p(t) \tag{1}$$

Spatial distribution of blast loading ($p(r)$) over the target surface is assumed to be uniform over the central part of the plate and exponentially decaying over the surrounding part of the plate [28], given as:

$$\mathrm{p(r)} = \begin{cases} 1 & 0 \le \mathrm{r} \le \mathrm{R_e} \\ \mathrm{ae^{-br}} & \mathrm{R_e} \le \mathrm{r} \le \mathrm{L} \end{cases} \tag{2}$$

Various functions are proposed to describe the pulse shape ($p(t)$) of a blast load. These include rectangular, triangular, sinusoidal, and exponentially decaying functions. While the dynamic plastic deformation of the plate has a strong dependence upon the pulse shape, Youngdahl [29] showed that these effects can be eliminated through introduction of effective pressure and impulse parameters. The pulse shape assumed in this work is a modified, non-dimensional form of Friedlander equation [30] given by Eq. (3). Thus, the parameters that fully define the loading profile are: p_0, t_d, α, b and R_e. It should be noted that the parameter $a = e^{bR_e}$ is not an independent parameter as it links the two functions proposed for the spatial distribution of loading.

$$p(t) = (1 - t/t_d\ )e^{-\alpha t} \tag{3}$$

It is assumed that the blast overpressure is laterally imparted on the target, that is, a quadrangular plate of characteristic side length L and characteristic thickness H, having the density ρ, made of ductile material of quasi-static yield stress σ_0, Young modulus E and gives rise to an axisymmetric displacement field of final central transverse deformation W_f. In this work, the dynamic flow stress is characterised by Johnson-Cook constitutive model given in Eq. (4).

$$\sigma'_y = [A_1 + B_1\varepsilon^n][1 + Cln(\dot{\varepsilon}^*)] \tag{4}$$

The expression in the first set of brackets gives the effect of material hardening without any strain rate effects (that is, at the reference strain rate $\dot{\varepsilon} = 1/s$), where $A_1 = \sigma_0$ is the static yield stress, $B_1$and n are the hardening constant and exponent, respectively. The expression abbreviated in the second set gives the effect of strain rate, where C is the strain rate sensitivity parameter and $\dot{\varepsilon}^* = \dot{\varepsilon}/\dot{\varepsilon}_0$ is the dimensionless plastic strain rate. While this model ignores the Bauschinger effect, it conveniently predicts the material behaviour which undergo strain hardening behaviour of isotropic materials. Thus, the parameters attributed to the material and geometric properties of the plate are $W_f,\ H,\ \rho,\ \sigma_0\ , L, B_1, E, \dot{\varepsilon}$.

By applying Buckingham's Pi-theorem, a system of 17 independent variables leaves a kernel of 14 dimensionless Π parameters, as defined by Eq.'s (5)-(18):

$$\Pi_1 = \frac{W_f}{H} \tag{5}$$

$$\Pi_2 = bD_e \tag{6}$$

$$\Pi_3 = \frac{p_0\sqrt{Q_e}t_d^3}{M_e} \tag{7}$$

$$\Pi_4 = \frac{d}{D_e} \tag{8}$$

$$\Pi_5 = \frac{M_e}{D_e^3}\sqrt{\frac{Q_e}{\rho\sigma_0}} \tag{9}$$

$$\Pi_6 = \frac{D_e}{\sqrt{Q_e}t_d} \tag{10}$$

$$\Pi_7 = \alpha t_d \tag{11}$$

$$\Pi_8 = L/H \tag{12}$$

$$\Pi_9 = \frac{R_e}{D_e} \tag{13}$$

$$\Pi_{10} = R_e/L \tag{14}$$

$$\Pi_{11} = \frac{E}{B_1} \tag{15}$$

$$\Pi_{12} = \frac{\rho D_e^3}{M_e} \tag{16}$$

$$\Pi_{13} = \frac{B_1}{\rho Q_e} \tag{17}$$

$$\Pi_{14} = \dot{\varepsilon} t_d \tag{18}$$

Through some algebraic manipulation, it can be seen that the unknown parameters of $p_0, b,\ t_d, \alpha, R_e, W_f,$ parameters are related to the ratio $\left(\frac{d}{D_e}\right)$ as follows:

$$p_0 = \frac{EM_e}{\rho D_e^3} f_1\left(\frac{d}{D_e}\right) \tag{19}$$

$$b = \frac{1}{D_e} f_2\left(\frac{d}{D_e}\right) \tag{20}$$

$$t_d = \frac{D_e}{\sqrt{Q_e}} f_3\left(\frac{d}{D_e}\right) \tag{21}$$

$$\alpha = \frac{\sqrt{Q_e}}{D_e} f_4\left(\frac{d}{D_e}\right) \tag{22}$$

$$R_e = L f_5\left(\frac{d}{D_e}\right) \tag{23}$$

$$\frac{W_f}{H} = \frac{M_e}{\rho D_e^3} f_6\left(\frac{d}{D_e}\right) \tag{24}$$

The dimensionless functions are obtained by regression analyses on the results of a series of numerical studies. It should be mentioned that, as ARMOX steel is less sensitive to strain rate effects ($C = 0.014$ in Table 1), the effect of material strain rate sensitivity is not considered in this study.

3. MATERIALS AND MODELS

3.1. Simulation of air and explosive

For the air blast loading, the space was initially filled with air, modelled as an ideal gas with the following equation of state:

$$P = (C_p - C_v)\rho_a T \tag{25}$$

where P is the gas pressure, $C_p = 1.005$ kJ/KgK and $C_v = 0.7176$ kJ/KgK are the specific heat parameters at constant pressure and volume, respectively, $\rho_a = 1.228$ kg/m^3 is the air density and $T = 289$ K is the gas temperature [31].

For the air blast explosion, the explosive was modelled by Jones -Wilkins-Lee Equation of state as:

$$P = A\left(1 - \frac{\omega\rho}{R_1\rho_0}\right)e^{-R_1\frac{\rho_e}{\rho_p}} + B\left(1 - \frac{\omega\rho}{R_2\rho_0}\right)e^{-R_2\frac{\rho_e}{\rho_p}} + \frac{\omega\rho^2}{\rho_0}E_{m0} \tag{26}$$

where ρ_p is the density of the explosive product, ρ_e is the density of the explosive at the beginning of process, A, B, R_1, R_2, and ω are the material constants [31], and E_{m0} is the specific internal energy, as presented in Table 1. In this study, the blast wave is generated by detonation of $40gr$ PE4 disc plastic explosive having the characteristic dimensions $D_e = 50mm$ and charge height calculated as $h_e = \frac{4M_e}{\rho_e \pi D_e^2} = 12.73mm$. The detonation is assumed to initiate from the centre of the explosive mass. The value of specific heat energy Q_e for PE4 is taken from Ref [32].

3.2. Steel material characterisation

ARMOX 440T is a type of high strength armour steel alloy manufactured by SSAB® which exhibits excellent tensile strength and blast resistance. The material properties of ARMOX 440T steel was taken from the bilinear quasi-static tests conducted at Imperial College Laboratory (Fig. 1) and ARMOX 44T data sheet [34]. Johnson- Cook Constitutive model was used to represent the dynamic flow stress, as in Eq. (4). The Johnson-Cook parameters for ARMOX 440T steel are obtained from Ref. [33] and presented in Table 1.

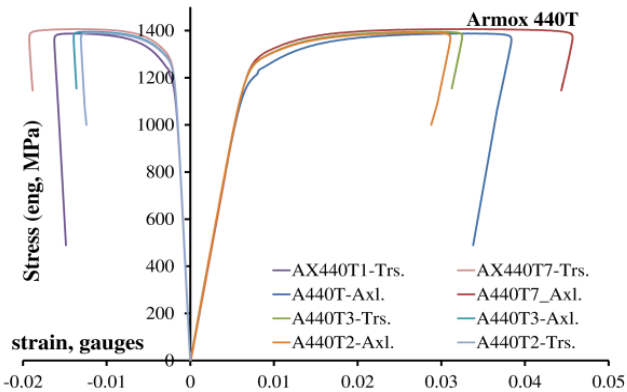

Fig. 1- Bilinear quasi-static plot of axial (Axl.) and transverse (Trs.) stress for ARMOX 440T

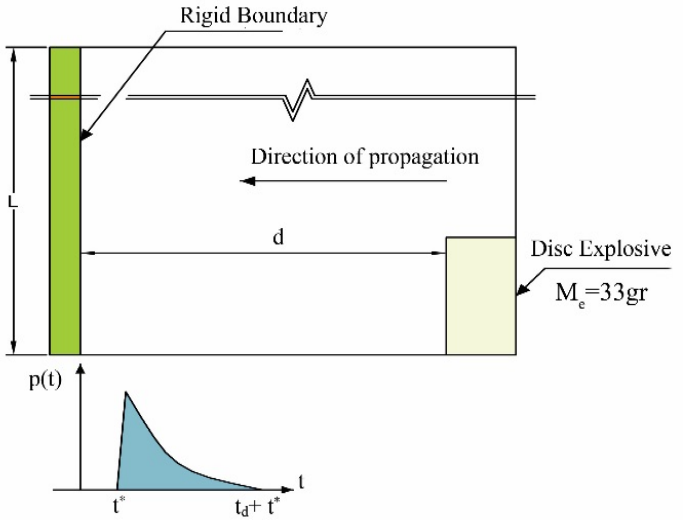

Fig. 2- Multi-material arrangement in Eulerian medium- t^* denotes the arrival time of the wave pressure at the boundary

Table 1- Material properties of air, plastic explosive and Steel plate(after Ref [33])

Material	ρ_e(kg/m^3)	Det. Wave speed v (m/s)	A (GPa)	B (GPa)	R_1 R_2	ω	E_m (kJ/kg)	Pre-det. bulk modulus
PE-4	1601	8193	6.0977×10^{11}	1.295×10^{10}	4.5 1.4	0.25	6.057×10^{6}	0
Air	**ρ_a(kg/m3)**	**μ_k $(\mu Pa.s)$**		**P (Pa)**	**E_0**		**$C_p - C_v$ Specific heat constant (at high temp) (Jkg^{-1}K^{-1})**	
	1.293	18.27		101325	2.5×10^{-4}		287	
ARMOX 440T Steel	**$A_1(MPa)$**	**$B_1(MPa)$ C**	**n**	**L (mm)**	**ν**	**E (GPA)**	**H (mm)**	**ρ (kg/m^3)**	**ε_f**
	1210	1543 0.014	0.584	400	0.3	200	4.61	7850	0.06

3.3. Description of experimental setup

The experimental tests on ARMOX steel panels have been carried out by Ref.'s [33], and [35] in Blast Impact and Survivability Research Unit at the University of Cape Town the details of which could be found in the literature, however; a brief description of the tests is given here. Air blast load was generated by the blast chamber facility through detonating disk explosives of PE4 using MA2A3 electrical detonator, which was in turn mounted on a polystyrene bridge to provide the desired stand-off by varying the lengths of bridge legs (Fig. 3). The panels were mounted on a modified pendulum system, as shown in Fig. 4, not only to determine the impulse but also to accommodate two high speed cameras to monitor the transient measurements for the plate. The plate was clamped along its periphery and the rear surface was painted with speckle pattern, utilised in the Digital Image Correlation (DIC) procedure. Full description of the experimental setup is given in Ref.'s [7], and [35], including experimental tests with various charge masses and with a horizontal pendulum. Table 2 summarises the experimental tests selected for this study. While AX440T with 38mm stand-off was used for validation, the other two models were employed to investigate the energy absorbing effectiveness factor discussed in Section 5.

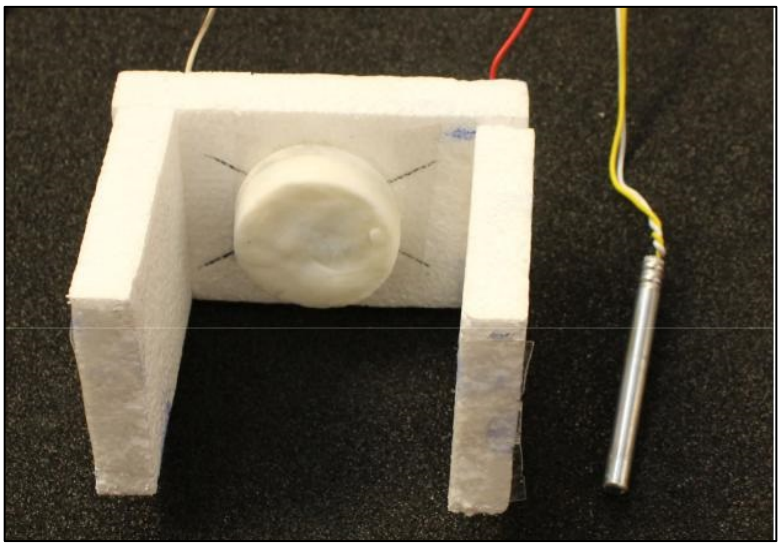

Fig. 3- Photograph of the loading arrangement

Fig. 4- Photograph showing the inside of the modified pendulum, set up for filming the rear surface of the plates

Table 1- Experimental tests data on ARMOX 370T and ARMOX 440T, with $\boldsymbol{D_e} = \boldsymbol{50mm}$. *Results of Ref [7]

Test Configuration	d	M_e	W_f	Impulse (N.s)	Failure mode	Pendulum type
AX370T	25	40	29.5*	80	II (partial tearing)	Horizontal
AX440T	25	60	Crack length 81mm	117.2	II	Horizontal
	38	33	13.5*	57.1	I	Modified swing

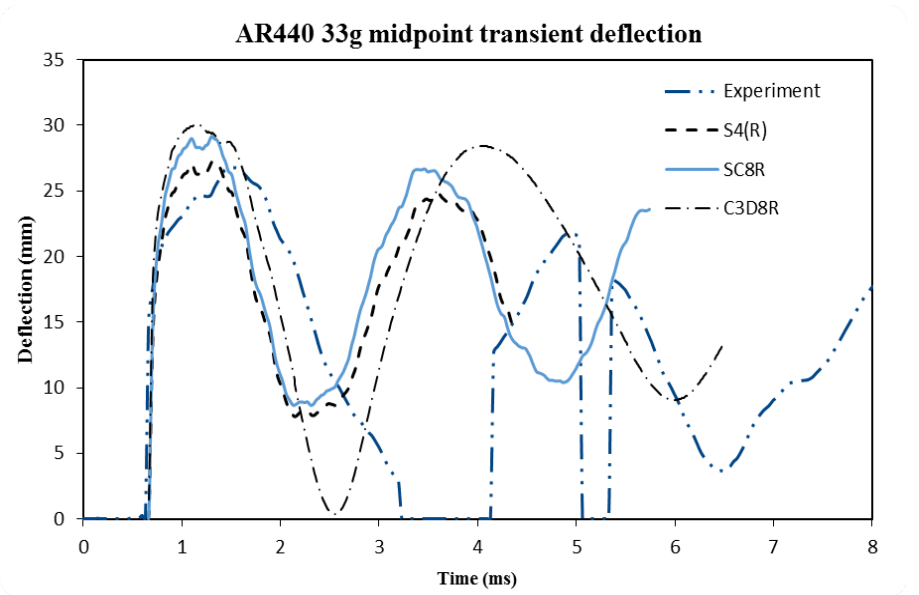

Fig. 5-Transient deformation of the panel (d=38mm, De=50mm, Me=33gr)

3.4. Numerical models

A preliminary numerical scheme is developed using the Multi Material Arbitrary Eulerian (MMAE) technique. The MMAE utilises continuum mechanics algorithms to obtain the solutions for the arbitrary motion of fluid mesh points relative to the (fixed reference) Eulerian points. In other words, a material Eulerian element may contain different material points and the mesh does not necessarily follow the motion of material. This technique, when coupled with Lagrangian model, is referred to as MMALE hereinafter, can trace the deformation and deformation gradients of the target by conservation of momentum in the contact pair surfaces between the target surface and the explosive product. MMALE is similar to MMAE but in MMALE the fluid interacts with the deformable target surface, enabling it to slide through the Eulerian mesh.

A 3D Eulerian cuboid of size 300x300x200, containing air and explosive, was set up in FE hydrocode ABAQUS 6.13, and meshed with ascending element lengths of 2mm in the vicinity of the explosive to 10mm furthest from the region of interest. The choice of element size serves a few purposes: for convergence of the pressure load, to ascertain adequate number of material mesh points are encompassed within the explosive material, and to reduce the computational costs. The outflow boundary was assigned to the top face and side faces of the cuboid, while the bottom face was assigned rigid boundary conditions. Fig. 2 shows the arrangement of this numerical model.

A total set of 9 simulations were conducted for the range of $0.5 \leq \frac{d}{D_e} \leq 3$, which consist of six simulations with incremental stand-off change of 25m, as well as stand-off values of 27, 30, 38mm. In crude terms, using the Hopkinson- Cranz law, this range corresponds to the full-scale spherical IED (Improvised Explosive Device) threats having diameter range of 70-700mm at 300-500mm stand -off, assuming the spherical and cylindrical explosives to have the same mass to generate the same pressure load.

For each test, the inflow of pressure, varying radially from the centre of the target, was quantified along the rigid target gauge points. Fig. 8 shows the advection of the explosive and fluid surface interaction at different times, while in Fig. 6 and Fig. 7 the pressure history at different gauge points is monitored.

3.5. Validation of numerical models

The complex nature of the localised blast phenomenon renders the prediction of the actual dynamic solution and associated damage modes in FE analyses intrinsically difficult. Accurate prediction of the structural response in FE models depends, firstly, on the accuracy of the mesh type to trace the solutions for local forces and bending moments along its section; and secondly, on the credibility of the input parameters utilised in the continuum mechanics equations incorporated in the FE computer programme. Unfortunately, more often than not, the coefficients are obtained empirically and vary in the literature. The plethora of values necessitate applying the consistency tests and validation of numerical models with experiments.

For this purpose, the transient deformation of the panel is investigated using MMALE analyses. The target surface in each analysis is discretised with different element type. This approach is similar to the one discussed in Section 3.1 but on deformable plate with material data presented in Table 1. Due to symmetry, only a quarter of the plate was integrated into the model with symmetry boundary conditions applied on the related segments of the boundary. An additional 20mm width was considered for two upper and lower clamps, modelled as rigid body surfaces and placed along the periphery of the plate. A penalty contact formulation was used with friction coefficient of 0.3 between the contact surfaces while contact between the plate and air was assumed frictionless.

In each set of simulations, the plate was discretised with a different element type, namely shell, membrane and continuum (solid homogeneous) elements, but with the same degree of refinement as 5mm element length (which satisfied the convergence). The shell elements used were conventional shell S4R and continuum shell SC8R elements. S4R elements are general purpose, uniformly reduced integration elements with hourglass control to avoid spurious zero energy modes. These elements allow for the finite membrane strains and arbitrary large rotations. The continuum shell elements (SC8R) on the other hand, are 8 noded hexahedral elements for general shell-like structures with continuum topology, adaptable to thick and thin shells, which allow for large strains and more accurate for contact pairs investigations.

The C3D8R continuum elements are a class of solid elements with reduced integration also known as ‘brick’ elements. These elements require refinement to capture stress components at boundary but are not stiff enough in bending unless a sufficient number of them are employed through the thickness of the plate/shell. The choice of 5 elements through thickness, in combination with enhanced hourglass control, is assumed to give reasonable estimate to capture the local bending.

Membrane elements (M3D8R) are 8 noded quadrilateral elements with reduced integration and hourglass control, which conform to simplified shell theory in which internal bending moments are neglected [36].

The element size in each model was kept constant at 5mm. The transient deflection of each model is validated against that of experiments in Fig. 5, which shows the permanent and maximum deformation at the centre of the panel are consistent with those of the shell elements. Table 3 shows the percentage of error in maximum deflections against experiment. The MMALE models were carried out on a cluster of 16 high performance CPU’s each having 1600MB memory.

The membrane elements experienced large out-of-plane deformations compared to all other element types. Due to the membrane element's paucity of bending stiffness perpendicular to its plane; the element convergence is fraught with difficulty due to excessive lateral deformations. It transpires from Fig. 5 and Table 3 that the conventional and continuum shell elements incur less computational cost than the membrane or continuum elements. Thus, the conventional shell elements can be used throughout the study.

Table 2- permanent and maximum transverse deformation of ARMOX Model ($\boldsymbol{M_e = 33gr, d = 38mm}$)

Element type	W_f (mm)	W (mm)	% Error W_f	% Error W	CPU Time (min)
C3D8R	18.73	30.98	28.53	12.3	173
S4(R)	16.10	27.27	10.47	1.83	63
SC8R	17.64	29.11	20.11	8.67	53
Experiment	13.5	26.78	NA	NA	NA

4. RESULTS AND DISCUSSIONS

4.1. Dimensionless parameters

Using the curve fitting tool in MATLAB, a set of dimensionless functions are obtained as presented in Eq.'s (27) - (34), and illustrated in Fig. 10 - Fig. 16 for the charge mass of 40gr. For the sake of comparison, the results of simulations with 60gr charge (19mm charge height) are also plotted in Fig. 11.

$$f_1 = 0.11\left(\frac{d}{D_e}\right)^{-1.153} \tag{27}$$

$$f_2 = 4.591\left(\frac{d}{D_e}\right)^{-0.42} \tag{28}$$

$$f_3 = 21.56\left(\frac{d}{D_e}\right) + 54.3 \tag{29}$$

$$f_4 = \frac{0.359}{\left(\frac{d}{D_e}\right)+2.138} \tag{30}$$

$$f_5 = 0.0363\ln\left(\frac{0.4d}{D_e}\right) + 0.0819 \tag{31}$$

$$f_6 = 344.8e^{-1.753\left(\frac{d}{D_e}\right)} \tag{32}$$

As the characteristics of loading variables (spatial and temporal) are known a priori, the transverse deflection of the plate in Eq. (24) due to such a load is measured by implementing the load in a separate full 3D pure Lagrangian analysis. In this model, a 3d matrix of the magnitude of pressure load with respect to its generalised coordinates is generated for each model, applied directly onto the panel with aforementioned geometry and properties as

discussed in Section 3.2, with rigid boundaries along its periphery. Due to symmetry, only a quarter of the plate is modelled. The panel is discretised with S4R shell elements of 5mm length and hourglass control to ensure convergence. Fig. 9 shows the maximum displacement of the two panels at varying stand-off.

Eq. (24) can be recast in the form of Eq. (33), where I^* is the impulse density (impulse per unit area). Thus, the dimensionless function attributing response to the impulse is given in Eq. (34) and plotted in Fig. 16. Table 4 summarises the impulse obtained in MMAE method using Eq. (36), over the radial distance (R) of 200mm.

$$\frac{W_f}{H} = \frac{I^*}{H\sqrt{\rho\sigma_0}} f_7\left(\frac{d}{D_e}\right) \tag{33}$$

$$f_7 = -2.036\left(\frac{d}{D_e}\right) + 10.08 \qquad 0.5 \le \frac{d}{D_e} < 0.75$$

$$f_7 = 4.28\left(\frac{d}{D_e}\right)^{-2.5} + 0.1 \qquad 0.75 \le \frac{d}{D_e} \le 3 \tag{34}$$

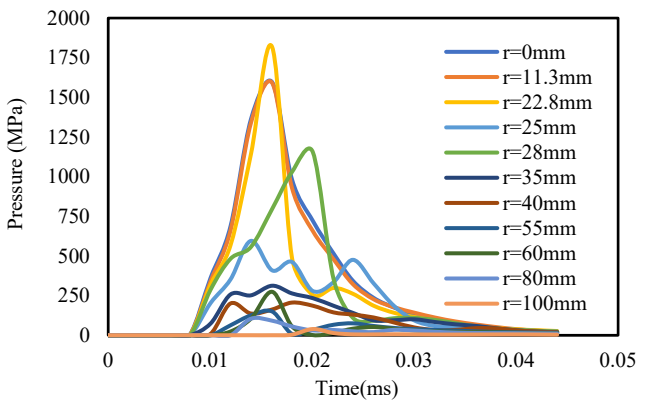

Fig. 6 Pressure load at various radial local coordinates ($\boldsymbol{d/D_e = 0.25}$)

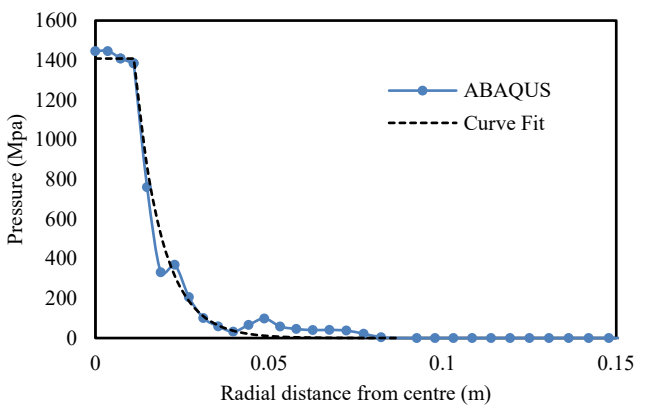

Fig. 7 Curve fit of pressure load across the target ($\boldsymbol{d/D_e = 0.54}$)

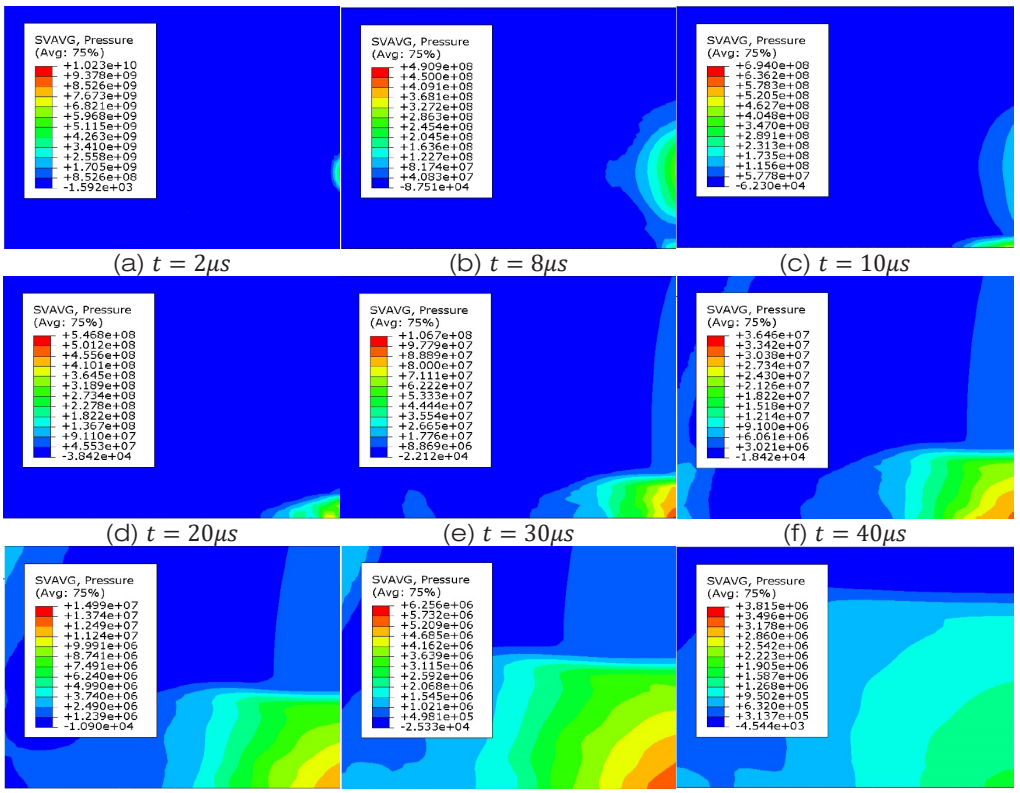

Fig. 8- Advection of the blast wave from 40gr explosive in air medium at 25mm stand-off

Table 3- Mid-point deflection vs impulse of MMALE models for ARMOX 440T

Test Number	d/D_e	Impulse (I) (N.s)	Test Number	d/D_e	Impulse (I) (N.s)
1	0.5	65.11	5	1	51.78
2	0.54	59.87	6	1.5	44.41
3	0.6	56.68	7	2	33.99
4	0.76	54.52	8	2.5	24.82
			9	3	22.55

In the case of proximal blast loads with $\frac{d}{D_e} \leq 1.5$, an incremental decrease in the abscissa leads to an abrupt increase in the ordinate of Fig. 10 and Fig. 15, marking a transition point in the type of response of target plate. Beyond $d/D_e = 1.5$ the blast load is projected more uniformly onto the plate surface, therefore deformation and the profile shape of the plate shifts from a local to a more global mode. It also transpires that, in the lower range stand-off the work done by external loads is less dispersed throughout the target surface, leading potentially to partial or total damage in the central region.

As observed in Fig. 11, the load decay constant (b) is linearly proportional to the charge mass. Thus, considering the mass of explosive and the air medium in which the blast wave

propagates, Eq. (20) can be modified as $b = \frac{M_e}{D_e^2 \rho_a} f\left(\frac{d}{D_e}\right)$. Combining this expression with Eq. (28)

$$f'_2\left(\frac{d}{D_e}\right) = \frac{D_e^3 \rho_a}{M_e} f_2\left(\frac{d}{D_e}\right) \tag{35}$$

The predicted normalised data from Fig. 11 for 60gr charge compares favourably with the data for 40gr charge, when combined with Eq. (35), as presented in Fig. 17.

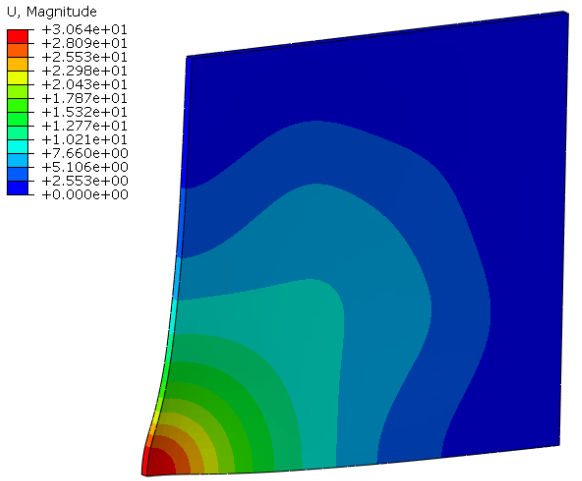

(a)

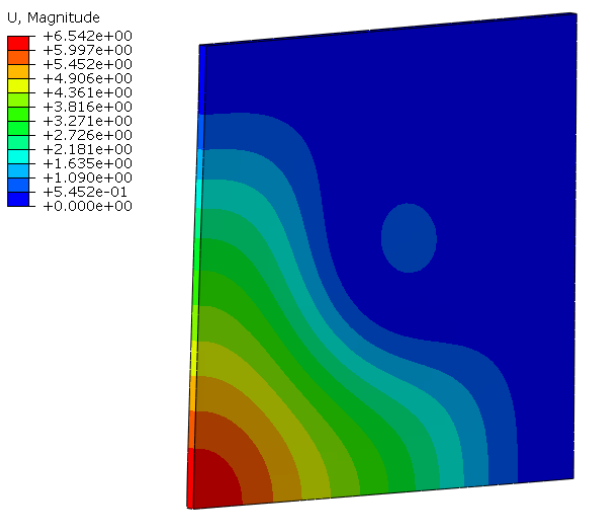

(b)

Fig. 9- Maximum deformation of the panels with (a) $\boldsymbol{d/D_e = 0.5}$ and (b) $\boldsymbol{d/D_e = 2}$

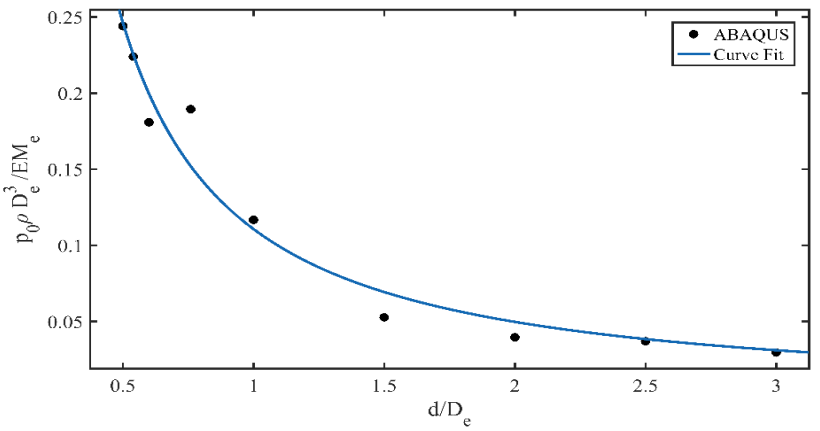

Fig. 10- Dimensionless pressure load (Equ. (27))

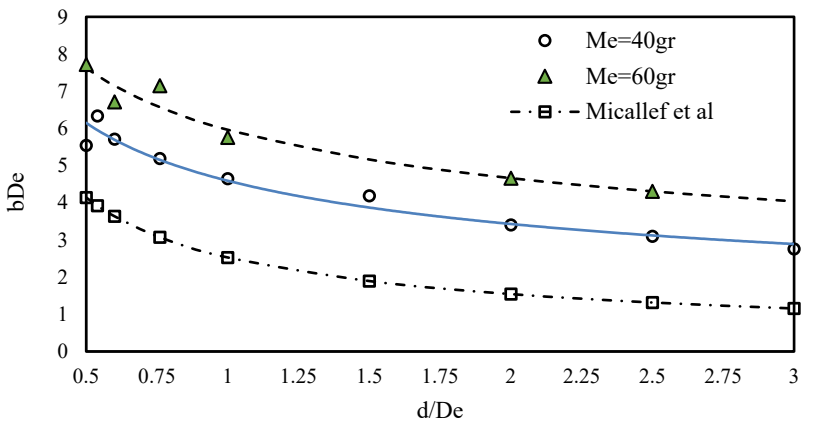

Fig. 11- Dimensionless load shape decay constant (Equ. (28))

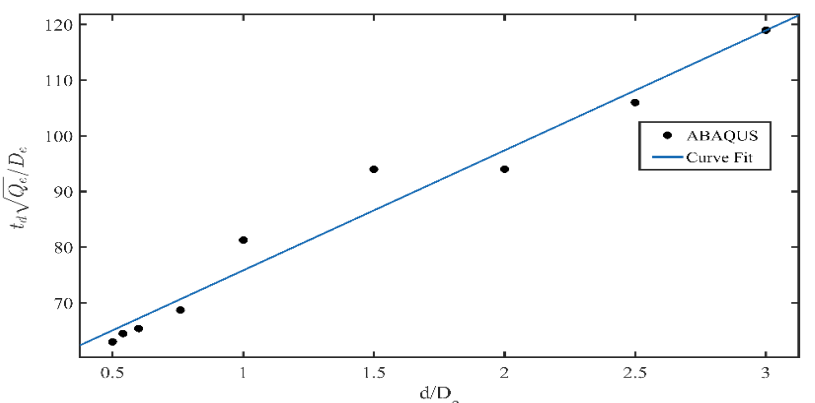

Fig. 12- Dimensionless paraments relating the duration of the load (Equ. (29))

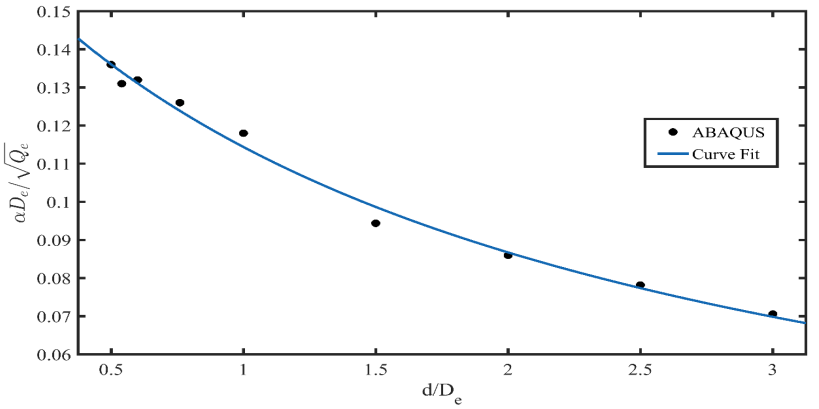

Fig. 13- Dimensionless pulse shape decay constant $\boldsymbol{\alpha}$ (Equ. (30)

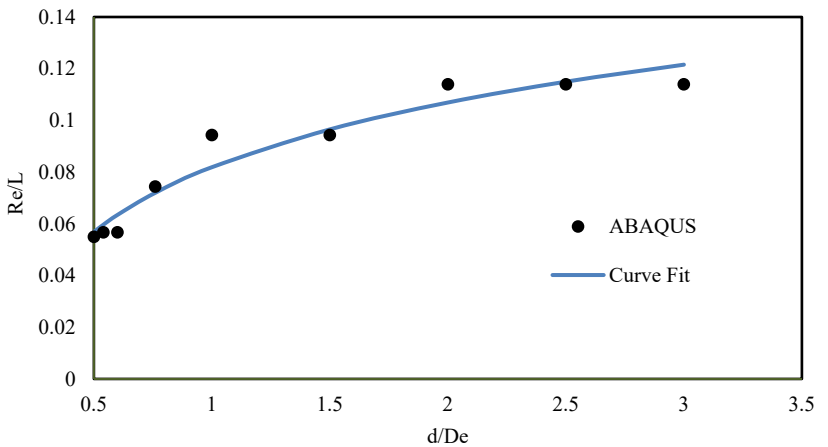

Fig. 14- Dimensionless $\boldsymbol{R_e}$ (Equ. (31))

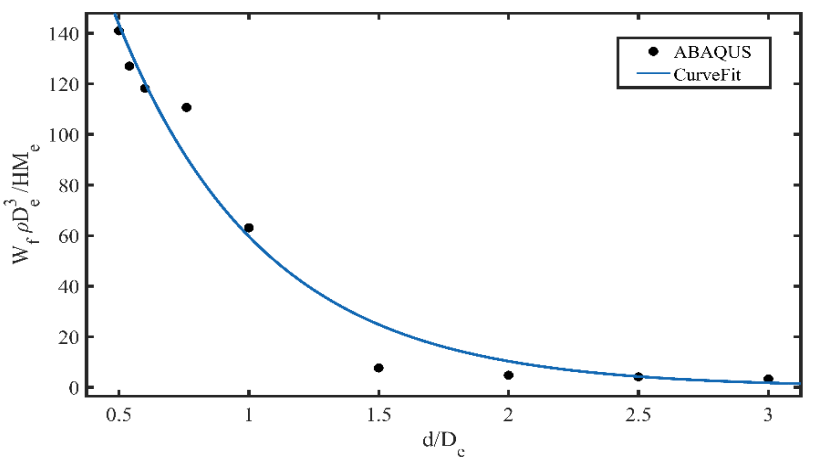

Fig. 15- Dimensionless permanent deflections of the plate (Equ. (32))

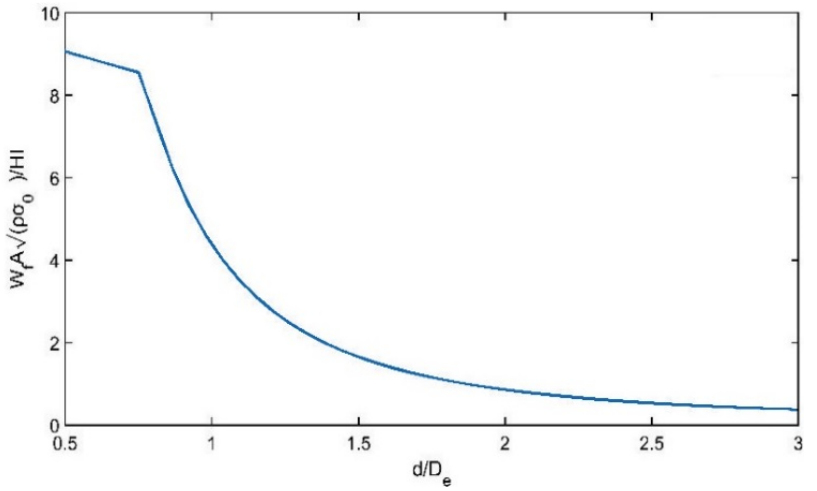

Fig. 16 -Curve fit of normalised displacement-impulse (Equ. (34))

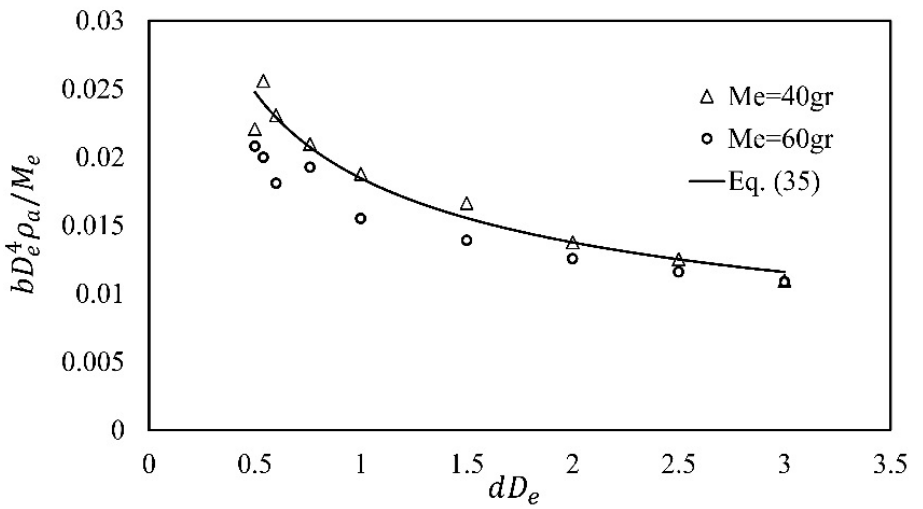

Fig. 17- Normalised data of load decay parameter

4.2. Impulsive loading

Eq. (36) gives the impulse imparted to the plate from the centre of projection to the characteristic radial distance $r^* = r$ from centre:

$$I(r) = 2\pi \int_0^{t_d} \int_0^r p(r^*, t) r^* dr^* dt^* \tag{36}$$

Assuming the impulse imparted over the square surface target of characteristic side length L is equivalent to a circular target of radius R, and defining $\lambda_0 = R_e/L$ and $\lambda = r/L$, we integrate Eq. (36) to give:

$$I(\lambda) = \begin{cases} \frac{\pi p_0\left(1+\alpha t_d - e^{-\alpha t_d}\right)(\lambda_0 bL)^2}{t_d \alpha^2} & \lambda < \lambda_0 \\ \frac{\pi p_0\left(1+\alpha t_d - e^{-\alpha t_d}\right)}{t_d \alpha^2}\left((\lambda_0 L)^2 + \frac{2e^{\lambda_0 Lb}}{b^2}\left(e^{-\lambda_0 Lb}(1+\lambda_0 Lb) - e^{-\lambda bL}(1+\lambda Lb)\right)\right) & \lambda \geq \lambda_0 \end{cases} \quad (37)$$

The total impulse that the charge could potentially impart to the target would thus be given by:

$$I(\infty) = \lim_{\lambda \to \infty}\{I(\lambda)\} = \frac{\pi p_0\left(1+\alpha t_d - e^{-\alpha t_d}\right)(\lambda_0 L)^2}{t_d \alpha^2} + \frac{2\pi p_0\left(1+\alpha t_d - e^{-\alpha t_d}\right)(1+\lambda Lb)}{t_d \alpha^2 b^2} \quad (38)$$

Thus, a non-dimensional impulse, i, can be defined as the quotient of the impulse imparted to a target over the total impulse that the blast can generate:

$$i = \frac{I(\lambda)}{I(\infty)} = \begin{cases} \frac{(\lambda_0 L)^2}{2+2\lambda_0 Lb+(\lambda_0 Lb)^2} & \lambda < \lambda_0 \\ 1 - \frac{2e^{-Lb(\lambda-\lambda_0)}[1+\lambda Lb]}{2+2\lambda_0 Lb+(\lambda_0 Lb)^2} & \lambda \geq \lambda_0 \end{cases} \quad (39)$$

Eq. (39) indicates the effectiveness of the plate to dissipate the impulse imparted to it which is usually measured against the total impulse required to penetrate the plate (rupture impulse or impulse threshold). As most blast scenarios studied here correspond to $60 < b < 120$, for the finite region of $0 < \lambda < 0.5$ the charge is 95% efficient (Fig. 18). Conversely, the reciprocal of Equ. (39) determines the efficiency of the charge, with $I(\infty)/I(\lambda) = 1$ indicating the full impulse imparted to the target.

The interaction surface of dimensionless impulse against stand off and λ (Fig. 19) suggests that for the blast loads generated by the same mass of explosive, the most threatening blast scenarios would be the small charge diameter and larger charge height, rather than high charge diameter and lower charge height. This is due to the nature of the detonation waves in a cylindrical explosive which propagate in the direction of its height. The pressure wave generated by the explosive product of larger height/diameter ratio would therefore concentrate on the centre of its projection on the plate, imparting more energy locally, thus possessing a higher value of surface traction hence a more localised penetrating effect. For example, within the finite region of $0 < \lambda < 0.5$, most localised blast load scenarios considered here correspond to the range of $60 < b < 120$, generating a potentially perforating impulse.

4.3. Energy absorbing effectiveness

A dimensionless energy absorbing effectiveness factor was introduced by Jones [37] as:

$$\psi = \frac{elastic\ and\ plastic\ strain\ energy\ absorbed\ by\ structural\ member}{enegy\ absorbed\ in\ the\ same\ volume\ of\ material\ up\ to\ failure\ in\ tension} \quad (40)$$

The denominator of Eq. (40) is the energy absorbed in the same volume of material up to rupture in a uniaxial tensile test specimen. The dynamic energy absorbing effectiveness factor was also defined, similar to Eq. (40) for the energy absorbing effectiveness factor subject to dynamic loads. Eq. (40) can be modified and rewritten as:

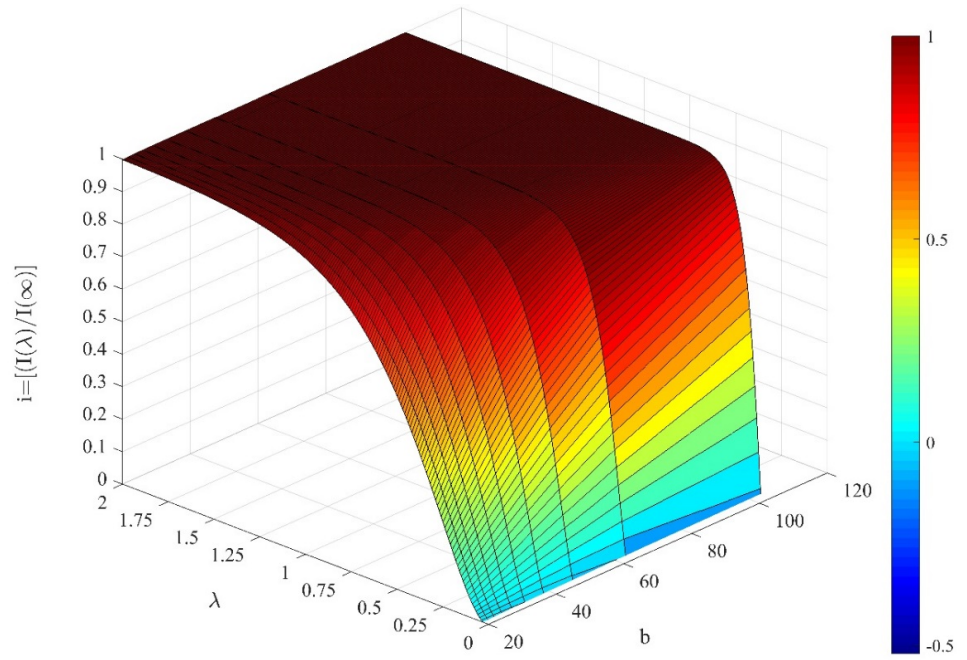

Fig. 18- interaction surface of the dimensionless impulse ***i***

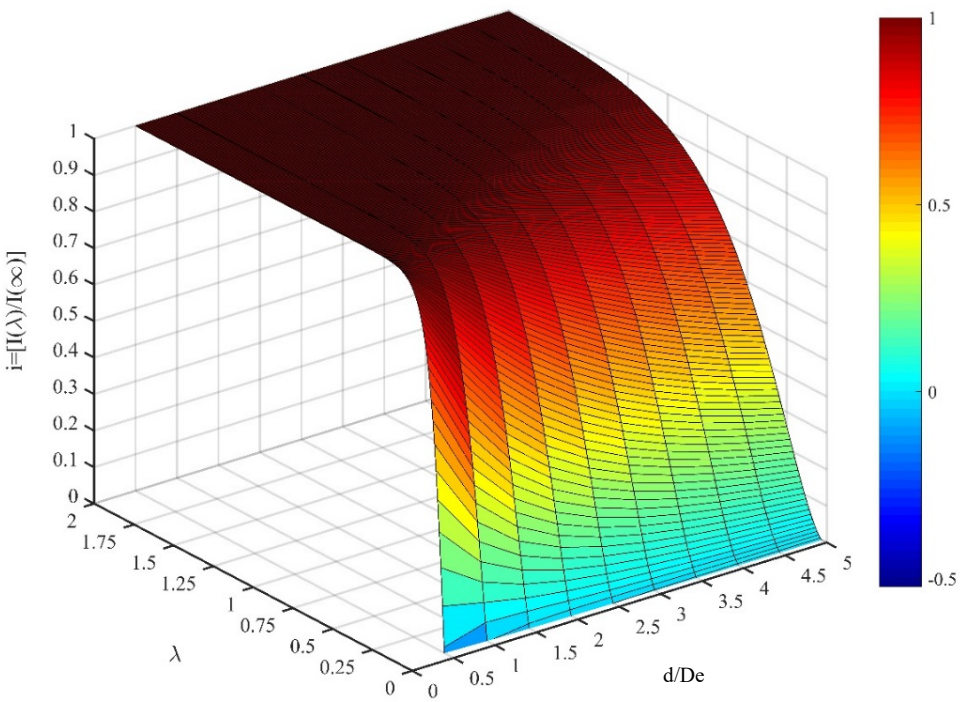

Fig. 19 interaction surface of dimensionless impulse i against normalised stand off

$$\psi' = \frac{\int_0^{\varepsilon_f} \phi(\varepsilon,\sigma_0,\dot{\varepsilon})\varepsilon d\varepsilon}{VU_{STF}} \tag{41}$$

Where $\phi(\varepsilon,\sigma_0,\dot{\varepsilon})$ is the strain rate dependent stress tensor of the material subject to dynamic loads, V is the volume of the material and $U_{STF} = 70MJ/m^3$ is the Specific Energy to Tensile Fracture of the material, which is the area under the stress strain curve of the material up to failure in the quasi-static test. Clearly, Eq. (41) can be used to determine the effectiveness of structure under various blast loading scenarios. For example, considering the blast generated by an explosive of $M_e = 60gr$, $d = 25mm$ and $D_e = 50mm$, the ARMOX 440T panel of 4.6mm thickness ruptured during the experiment (Table 2). Thus, the calculated energy absorbed effectiveness factor can be stipulated as the pivot threshold energy to predict rupture of various ARMOX440T panels, when subjected to various proximal or distal pressure waves at increased stand-off but generated with disc explosives of higher masses and (Fig. 20).

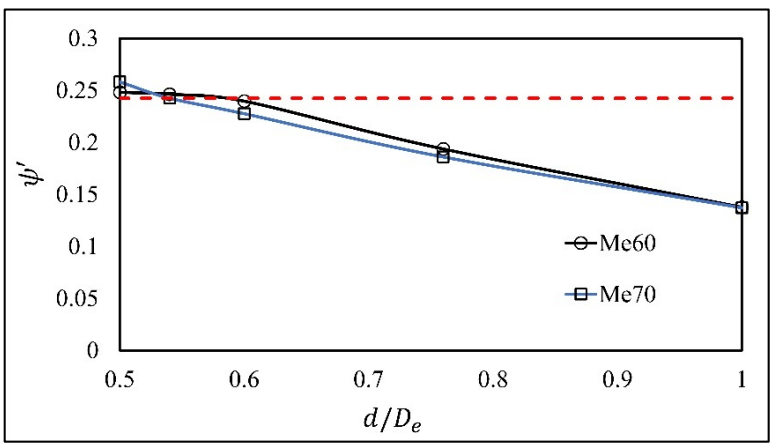

Fig. 19 -Dimensionless energy absorbing effectiveness factor $\boldsymbol{\psi'}$ for ARMOX 440T, the region of $\boldsymbol{\psi' > 0.248}$ correspond to the blast load which is predicted to penetrate the plate.

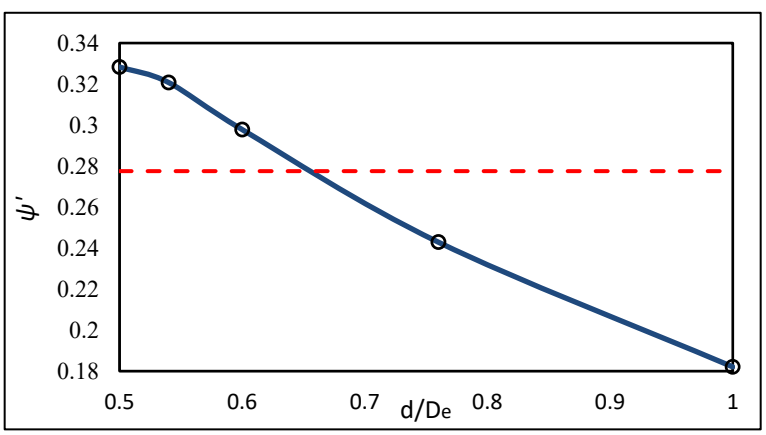

Fig. 20 - Prediction of the failure of ARMOX 370T panels with $\boldsymbol{M_e = 60gr}$ (____), using experimental result of ARMOX370T which exhibit Mode II failure (partial tearing at centre) with $\boldsymbol{M_e = 40gr}$, $\boldsymbol{d/D_e = 0.5}$ (_ _ _ _).

The data from the ARMOX 370T plates are graphed in Fig. 21. The plasticity in the plate was characterised by Johnson-Cook visco-plastic model with strain hardening and rate sensitivity given as in Table 1, with identical geometric properties to ARMOX 370T (Table 1) except with $H = 3.81mm$, $\sigma_0 = A_1 = 1157MPa$ and $\varepsilon_f = 8\%$. In this case, the threshold energy corresponds to loading parameters of $M_e = 40gr$, $d = 25mm$ and $D_e = 50mm$ [7], which ensued partial crack in the centre of the plate. Table 5 summarises the deformation and the predicted failure modes of the plates. Whether the panels with higher value of ordinate in Fig. 21 than those of the threshold energy will actually undergo mode II or mode III failure is not investigated here and requires further experiments.

CONCLUDING REMARKS

This article investigates the dynamic plastic response of localised blast loaded steel plates through dimensional analyses of the target and close-in blast loading. By assuming that the blast load, generated by cylindrical charge, consists of two independent parts (load shape and pulse shape), a set of 7 dimensionless functions are identified by applying the rank-nullity (Buckingham's Pi-) theorem. The functions were parametrised in terms of standoff/diameter ratio, and obtained in two stages, by a preliminary numerical method known as MMAE in ABAQUS and a regression analysis. The MMAE technique is based on the full interaction of the PE4 explosive products with the rigid structure, from which various loading parameters were obtained. The regression analysis performed on the scatter plots of the loading parameters identifies the form of dimensionless functions.

Preliminary results reveal that the trend of loading magnitude, and hence the trend of the plate deformation, shifts at the critical stand-off, demonstrating a shift in the sensitivity of the plate response to the projection of the blast. With more proximal blast, the projection of the blast is focused on the central part of the plate, leading to large deformations, higher deformation gradients and potential rupture of the plate.

The dimensionless parameters studied here provide a spectrum of data that can render the same trend for the response of full-scale prototype plates possessing the same values of dimensionless parameters as the small-scale models to blast loads, without having to perform rigorous blast testing on the physical panel prototype.

A series of further FSI simulations was performed using deformable target surface. Foremost, the transient deformation of a model was measured experimentally to validate the numerical models. The numerical models were compared against the experimental data, showing good agreements in terms of permanent and maximum deformations.

For experimental specimens with loading parameters that resulted in the rupture of the panels (Mode II failure), the dimensionless energy absorbing effectiveness factor was quantified numerically and utilised to predict the rupture of the plates for more distal blasts but increased charge heights (mass). This approach is useful to predict the failure modes of geometrically similar ARMOX prototype panels, on which the load is generated by a cylindrical PE4 charge, assuming the material properties remain constant during scaling.

Table 4- permanent and maximum transverse mid-point deflection of the plate from MMALE analysis

Test plate	d (mm)	Range of M_e (gr)	W_f (mm)	W (mm)	Predicted Failure mode
AX370T	25	40	29.5	42.93	II (from expt.)
	25	60	-(*)	47.12	II
	27		33.73	45.20	II
	30		31.82	43.65	II
	38		26.21	38.58	I
	50		20.33	32.90	I
AX440T	25	60	40.21	28.91	II (from expt.)
	27	60	38.80	27.59	I
	30	60	37.84	27.78	I
	38	60	33.90	23.27	I
	50	60	28.79	17.46	I

FUNDING

The authors received no financial support for the research, authorship or publication of this paper.

REFERENCES

[1] N. Jacob, S. C. K. Yuen, G. N. Nurick, D. Bonorchis, S. A. Desai, and D. Tait, "Scaling aspects of quadrangular plates subjected to localised blast loads - Experiments and predictions," Int. J. Impact Eng., vol. 30, no. 8–9, pp. 1179–1208, 2004.

[2] S. Chung Kim Yuen and G. N. Nurick, "The significance of the thickness of a plate when subjected to localised blast loads," Blast Impact Load. Struct., pp. 471–499, 2000.

[3] T. Wierzbicki and G. N. Nurick, "Large deformation of thin plates under localised impulsive loading," Int. j. Impact Engng, vol. 18, no. 96, pp. 899–918, 1996.

[4] G. N. Nurick and J. B. Martin, "Deformation of thin plates subjected to impulsive loading-a review -Part I: Theoretical considerations," Int. J. Impact Eng., vol. 8, no. 2, pp. 159–170, 1989.

[5] G. N. Nurick, M. D. Olson, J. R. Fagnan, and a. Levin, "Deformation and tearing of blast-loaded stiffened square plates," Int. J. Impact Eng., vol. 16, no. 2, pp. 273–291, 1995.

[6] F. Schneider and N. Jones, "Impact of thin-walled high-strength steel structural sections," Proc. Inst. Mech. Eng. Part D J. Automob. Eng., vol. 218, no. 2, pp. 131–158, 2004.

[7] G. S. Langdon, W. C. Lee, and L. A. Louca, "The influence of material type on the response of plates to air-blast loading," Int. J. Impact Eng., vol. 78, pp. 150–160, 2015.

[8] T. Børvik, S. Dey, and a. H. Clausen, "Perforation resistance of five different high-strength steel plates subjected to small-arms projectiles," Int. J. Impact Eng., vol. 36, no. 7, pp. 948–964, 2009.

[9] S. B. Menkes and H. J. Opat, "Broken beams - Tearing and shear failures in explosively loaded clamped beams," Exp. Mech., vol. 13, no. 11, pp. 480–486, 1973.

[10] G. N. Nurick and A. M. Radford, "Deformation and tearing of clamped circular plates subjected to localised central blast loads," Recent Dev. Comput. Appl. Mech. (Ed. B.D Reddy), vol. a volume i, pp. 276–301, 1997.

[11] N. Jacob, G. N. Nurick, and G. S. Langdon, "The effect of stand-off distance on the failure of fully clamped circular mild steel plates subjected to blast loads," Eng. Struct., vol. 29, no. 10, pp. 2723–2736, 2007.

[12] G. N. Nurick and J. B. Martin, "Deformation of thin plates subjected to impulsive loading - A review - Part II - Experimental results," Int. J. Impact Eng., vol. 8, no. 2, pp. 171–186, 1989.

[13] G. N. Nurick and G. C. Shave, "The deformation and tearing of thin square plates subjected to impulsive loads - An experimental study," Int. J. Impact Eng., vol. 18, no. 1, pp. 99–116, 1996.

[14] S. C. K. Yuen and G. N. Nurick, "Experimental and numerical studies on the response of quadrangular stiffened plates. Part I: Subjected to uniform blast load," Int. J. Impact Eng., vol. 31, no. 1, pp. 55–83, 2005.

[15] G. N. Nurick and V. . Balden, "Localised Blast Loaded Circular Plates: an Experimental and Numerical Investigation," Proc. IMPLAST 2010 Conf., vol. 12, no. 14, pp. 145–152, 2010.

[16] J. Smith, J. Doe, and J. Scientist, "Ductile Failure of the Steel plate subjected to localised blast loading numerical approach Science," pp. 1–7.

[17] D. Bonorchis and G. N. Nurick, "The analysis and simulation of welded stiffener plates subjected to localised blast loading," Int. J. Impact Eng., vol. 37, no. 3, pp. 260–273, 2010.

[18] W. Grobbelaar and G. Nurick, "An investigation of Struvctures Subjected to Blast Loads Incorporating an Equation of State to Model the Material Behaviour of the Explosives," in 7th International Symposium on Structural Failure and Plasticity (IMPLAST 2000), 2000, pp. 185–194.

[19] A. Chen, L. A. Louca, and A. Y. Elghazouli, "Blast assessment of steel switch boxes under detonation loading scenarios," Int. J. Impact Eng., vol. 78, pp. 51–63, 2015.

[20] T. Børvik, A. G. Hanssen, M. Langseth, and L. Olovsson, "Response of structures to planar blast loads - A finite element engineering approach," Comput. Struct., vol. 87, no. 9–10, pp. 507–520, 2009.

[21] S. Chung Kim Yuen, G. S. Langdon, G. N. Nurick, E. G. Pickering, and V. H. Balden, "Response of V-shape plates to localised blast load: Experiments and numerical simulation," Int. J. Impact Eng., vol. 46, pp. 97–109, 2012.

[22] B. Zakrisson, B. Wikman, and H. K. Häggblad, "Numerical simulations of blast loads and structural deformation from near-field explosions in air," Int. J. Impact Eng., vol. 38, no. 7, pp. 597–612, 2011.

[23] V. Aune, E. Fagerholt, K. O. Hauge, M. Langseth, and T. Børvik, "Experimental study on the response of thin aluminium and steel plates subjected to airblast loading," Int. J. Impact Eng., vol. 90, pp. 106–121, 2016.

[24] K. Spranghers, I. Vasilakos, D. Lecompte, H. Sol, and J. Vantomme, "Identification of the plastic behavior of aluminum plates under free air explosions using inverse methods and full-field measurements," Int. J. Solids Struct., vol. 51, no. 1, pp. 210–226, 2014.

[25] A. Neuberger, S. Peles, and D. Rittel, "Scaling the response of circular plates subjected to large and close-range spherical explosions. Part I: Air-blast loading," Int. J. Impact Eng., vol. 34, no. 5, pp. 874–882, 2007.

[26] A. Neuberger, S. Peles, and D. Rittel, "Scaling the response of circular plates subjected to large and close-range spherical explosions. Part II: Buried charges," Int. J. Impact Eng., vol. 34, no. 5, pp. 874–882, 2007.

[27] K. Micallef, a. S. Fallah, D. J. Pope, and L. A. Louca, "The dynamic performance of simply-supported rigid-plastic circular steel plates subjected to localised blast loading," Int. J. Mech. Sci., vol. 65, no. 1, pp. 177–191, 2012.

[28] A. S. Fallah, K. Micallef, G. S. Langdon, W. C. Lee, P. T. Curtis, and L. A. Louca, "Dynamic response of Dyneema® HB26 plates to localised blast loading," Int. J. Impact Eng., vol. 73, pp. 91–100, 2014.

[29] C. K. Youngdahl, "Influence of pulse shape on the final plastic deformation of a circular plate," Int. J. Solids Struct., vol. 7, no. 9, pp. 1127–1142, 1971.

[30] R. Rajendran and J. M. Lee, "Blast loaded plates," Mar. Struct., vol. 22, no. 2, pp. 99–127, 2009.

[31] D. Bonorchis and G. N. Nurick, "The influence of boundary conditions on the loading of rectangular plates subjected to localised blast loading - Importance in numerical simulations," Int. J. Impact Eng., vol. 36, no. 1, pp. 40–52, 2009.

[32] B. M. Dobratz, "Properties of Chemical Explosives and Explosive Simulants," Livermore, 1972.

[33] N. Mehreganian, L. A. Louca, G. S. Langdon, R. J. Curry, and N. Abdul-Karim, "The response of mild steel and armour steel plates to localised air-blast loading-comparison of numerical modelling techniques (Submitted for Publication)," Int. J. Impact Eng., 2017.

[34] SSAB, "Armox 440T Blast protection plate," 2017. [Online]. Available: http://www.ssab.co.uk/products/brands/armox/armox-440t.

[35] R. J. Curry and G. S. Langdon, "Transient response of steel plates subjected to close proximity explosive detonations in air," Int. J. Impact Eng., vol. 102, pp. 102–116, 2017.

[36] Dassault Systèmes Simulia, "Abaqus CAE User's Manual," Abaqus 6.12, p. 1174, 2012.

[37] N. Jones, "Energy-absorbing effectiveness factor," Int. J. Impact Eng., vol. 37, no. 6, pp. 754–765, 2010.

[38] K. Micallef, A. Soleiman Fallah, D. J. Pope, M. Moatamedi, L. A. Louca, and H. Road, "On dimensionless loading parameters for close-in blasts," Int. Jounral Multiphysics, vol. 9, no. 2, pp. 171–194, 2015.

NOMENCLATURE

B, L	[L]	plate characteristic lengths
B_1	[$ML^{-1}T^{-2}$]	Johnson Cook hardening parameter
C		Johnson Cook rate dependent coefficient [1]
C_p	[$L^2T^{-2}K^{-1}$]	ideal gas specific heat at constant pressure
C_v	[$L^2T^{-2}K^{-1}$]	ideal gas specific heat at constant volume
D_e	[L]	load diameter
E	[$ML^{-1}T^{-2}$]	Young's modulus
H	[L]	plate characteristic thickness
I^*	[$ML^{-1}T^{-1}$]	impulse density
I	[MLT^{-1}]	impulse transmitted to the plate
M_e	[M]	mass of explosive
Q_e	[$L^2\ T^{-2}$]	specific Heat Energy
R_e	[L]	radius of centrally loaded plate
B	[L^{-1}]	load shape explosive decay constant
d	[L]	stand-off distance,
he	[L]	charge height,
p_0	[$ML^{-1}T^{-2}$]	maximum explosive pressure,
R	[L]	characteristic radial distance from centre
α	[T^{-1}]	Pulse shape decay constant
$\dot{\varepsilon}$	[T^{-1}]	material strain rate,
E		material strain [1]
ε_f		strain at tensile fracture (% elongation) [1]
P	[ML^{-3}]	material density,
ρ_e	[ML^{-3}]	explosive density,
ρ_a	[ML^{-3}]	air density,
t_d	[T]	duration of the blast load,
μ_k	[$ML^{-1}T^{-1}$]	dynamic viscosity of air,
σ_0	[$ML^{-1}T^{-2}$]	material static yield stress,
σ'_y	[$ML^{-1}T^{-2}$]	material flow stress,
σ_{UT}	[$ML^{-1}T^{-2}$]	ultimate static tensile stress,
ψ'		energy absorbing effectiveness factor, [1]